Journal of Materials Science: Materials in Electronics (2019) 30:5470–5477
https://doi.org/10.1007/s10854-019-00840-0

Structural, dielectric and ferroelectric properties of lead free Gd-modified $BiFeO_3$–$BaTiO_3$ solid solution

C. Behera[1,2] · A. K. Pattanaik[2]

Received: 26 November 2018 / Accepted: 28 January 2019 / Published online: 7 February 2019

Abstract
Due to the high Curie temperature the rare-earth-modified bismuth ferrite ($BiFeO_3$ or BFO) and/or its derivatives have uncomplicated lead-free chemistries and simple perovskite structures have attracted the materials community. So, in this report, structural, micro-structural, ferroelectric and electrical characteristics of a rare-earth (Gd)-modified perovskite $BiFeO_3$–$BaTiO_3$ solid solution, fabricated by a cost effective solid-state reaction technique, have been presented. The structural analysis using X-ray diffraction pattern and data indicates the evolution of a mono-phase distorted perovskite structure with the existence of rhombohedral structure. The ambient temperature scanning electron micrograph of Gd modified $BiFeO_3$–$BaTiO_3$ solid solution exhibits uniform grain distribution over the surface. The dielectric parameters are found to be frequency and temperature dependent. The well defined polarization–electric field hysteresis loop of the samples at room temperature suggest that Gd substitution at the Bismuth site of the solid solution strongly affects remnant and saturated polarization of the materials. The ac conductivity spectra obeys the Jonscher's power law. Based on the derived parameters of Gd modified $BiFeO_3$–$BaTiO_3$ solid solution, it is expected to fabricate a functional device.

1 Introduction

Last few decades have witnessed the booming demand to develop materials for fabrication of multifunctional electronic devices. For the purpose, material with diverse functional microscopic order parameters, such as charge, spin, lattice and orbital, could be more prospective for new types of multifunctional electronic devices including memory devices, sensors, and spintronics. Though coexistence of more than one order parameters with multi-phenomenon (i.e., ferromagnetism, ferroelectricity and ferroelasticity) in a single phase material is found be very useful but their number is still not high [1]. Hence, people are paying much more attention to develop such type of materials. Now being the age of marching towards lead-free environment friendly materials for the safety measure of the operation and handing, it is urgent to pay much attention on the development of new lead-free materials with noticeable piezoelectric, strong multiferroic and good temperature stability properties. In this line mono-phase $BiFeO_3$ (BFO) has gained special attention of the researcher owing to its novel multiferroicity at ambient temperatures with excellent properties, like $T_N = 347–397$ °C, Tc = 807–877 °C [2]. However, couple of its inherent problems of this material have restricted to synthesize mono-phase BFO. It is because of the determination of precise temperature domain for phase stabilization, as a result, a few secondary phases (i.e., $Bi_2Fe_4O_9$, $Bi_{25}FeO_{39}$, etc.) are generally formed. In addition to this, the reduction of Fe^{3+} to Fe^{2+} (i.e., $4Fe^{3+} + 2O^{2-} \rightarrow 4Fe^{2+} + O_{2g}$) and formation of oxygen vacancies during sintering lead to large leakage current in BFO and other related multiferroic materials [3]. Hence, people are trying to solve these inherent problems by adopting different strategies like introducing isovalent/non-isovalent elements in its *Bi and Fe* sites, or fabrication of solid solution or composites with prototype polar or non-polar structure to enhance its multiferroic properties to be fit for device application. It has also been reported that high-insulation BFO ceramics with pure perovskite phase can be synthesized by introducing the tetragonal ferroelectric phase into BFO which suppresses the above impurity phases and enhances its multiferroic properties [4]. For this purpose, lead-free perovskite ferroelectric $BaTiO_3$ (BT) has been found more suitable because of its

✉ C. Behera
cdbehera1986@gmail.com

[1] Department of Physics, National Institute of Technology, Agartala, Tripura 799046, India

[2] Department of Physics, V S S University of Technology, Burla 768018, India

excellent ferroelectric properties ($T_c = 120$ °C, $P_s = 26$ μC/cm^2 and $\varepsilon_r > 1000$) [5]. Many research work have already been reported on enhancement of multiferroic characteristics by several experimental strategy and using chemical leaching, rapid liquid phase sintering, etc. Beside this, partial replacement of comparable ions for Bi^{3+} or Fe^{3+} in the $BiFeO_3$, lattices namely Gd^{3+} [6], La^{3+} and Sm^{3+} [7] for Bi^{3+} and Al^{3+} [8] and Co^{3+} [9] for Fe^{3+} and fabrication of solid solution of BFO with $BaTiO_3$ [10, 11] have been found very fruitful for device applications. Extensive studies of BFO-based binary solid solutions, ($BiFeO_3$–$BaTiO_3$ (BFO–BT)) have mainly primarily been concentrated on both the dielectric and magnetic characteristics, and infrequently delineate saturated hysteresis of ferroelectric and piezo response and also be harmonize with their magnetic and electronic properties [2]. It is important to note that BFO–BT solid solution reported to have ferromagnetism, though both counterpart possess, one antiferromagnetic and another ferroelectric, at room temperature. In BFO–BT solid solution, the substitution of Ba^{2+} at the Bi^{3+} and Ti^{4+} at the Fe^{3+} sites leads to a complex structural change. Since the ionic radii of Ba^{2+} (1.56 Å) is larger than Bi^{3+} (1.17 Å), this difference in ionic radii induce iso-static pressure (chemical pressure) on the crystal structure, as a result, there is a change in crystal system of BFO, where the symmetry evolves to monoclinic or orthorhombic arrangement [12]. Detailed Literature survey reveals that the substitution of lanthanides (i.e., *La, Sm, Nd, Gd, Dy*, etc) at the Bi^{3+} site of the BFO has a number of important consequences, including change of the antiferromagneticity to ferromagnetism. Based on $BiFeO_3$–$XFeO_3$ (X = lanthanide) phase diagrams one can observe the significant influence of lanthanide species on the composition-structure relationship. It is also important that the amount of an intermediate non-polar orthorhombic (space group Pbam) phase that coexists with the polar rhombohedral R3c phase depending on both the lanthanide content. Similarly, the lanthanides vary the curvature of the phase boundary (i.e. the slope of the phase boundary in a temperature-composition phase diagram) between the polar rhombohedral R3c phase and the non-polar orthorhombic Pnma (or Pbnm) phase [referred to as a morphotropic phase boundary (MPB)]. This suggests that each *X*-species has a different influence on the polar-to-non-polar phase transition temperature for a given concentration of *X* [13]. In contrast, the ion substitution at the Bi^{3+} or/and Fe^{3+} sites in $BiFeO_3$ favours to enhance its piezoelectric responses, principally ion substitutions like La^{3+}, Sm^{3+}, Y^{3+}, Dy^{3+}, Pr^{3+}, Nd^{3+}, etc. for the Bi^{3+} site. Though some work has already been carried out in the lanthanide modified BFO–BT solid system, it was some difficult to prepare impurities-free BFO–BT solid solution. As a result it will hampered to get optimum multiferroicity (ferroelectric polarization and magnetization) [14]. In view of the important role of rare-earth substitution to solve the inherent problems (namely, enhancement of multiferroic properties and removal of some anomalies of the earlier reports), we have carried out the systematic work on synthesis and characterization of Gd-modified BFO–BT solid solutions. In this communication, an important role of Gd substitution on structural, dielectric, impedance, modulus, ferroelectric and transport properties of BFO–BT solid solution fabricated by standard cost effective solid state route have been reported.

2 Materials and methods

The polycrystalline solid solutions of Gd-modified $BiFeO_3$–$BaTiO_3$ having chemical compositions $(Bi_{0.45}Gd_{0.05}Ba_{0.5})$ $(Fe_{0.5}Ti_{0.5})O_3$ (here after named as BGFBT) along with $BaTiO_3$(BT) and $BiFeO_3$ (BFO) has been synthesized using a standard cost effective high-temperature solid-state reaction technique [15, 16] by taking high-purity analytical grade ingredient purchased from Merck of oxides or carbonate; namely bismuth oxide Bi_2O_3, iron oxide Fe_2O_3, barium carbonate $BaCO_3$, titanium dioxide TiO_2 and gadolinium oxide Gd_2O_3 in a required stoichiometry. A small amount (4%) of extra Bi_2O_3 [17] has been added to the mixture of the above compounds to prepare the solid solution in order to compensate the loss of bismuth during the high-temperature processing. All the ingredients were ground thoroughly by dry (air) as well as wet (methanol) mode in an agate mortar and pestle for 2 h. The homogeneously mixed powders were calcined at the optimized temperature in temperature of 980 °C (for BGFBT), 780 °C (for BFO) and 1150 °C (for BT) for 6 h in a covered alumina crucible. The diffraction patterns and data of the calcined powders were obtained by X-ray powder diffractometer of M/s Bruker (model D8 Advance) with wavelength 1.5418 Å in a slow speed scan mode (rate of scanning = 1°/min). The pellets of a small dimension (10 mm diameter and 1–2 mm thickness) were fabricated using polyvinyl alcohol PVA as binder mixed powders by a KBR hydraulic press at 7×10^7 kg/m^2 pressure. The sintering of the pellets of the compounds was carried out in the temperature of 1060 °C (for BGFBT), 800 °C (for BFO) 1200 °C (for BT) for 4 h in the alumina crucible. For electrical measurements, highly conducting silver paste (purchased from Sigma Aldrich) was painted on the flat and parallel surfaces of the sintered pellets, and annealed at 200 °C for 12 h. The dielectric and related parameters were measured over a wide range of frequency (50 Hz–1 MHz) and temperature by a LCR meter (model Agilent E4980A of M/s Agilent Technologies Inc.). In order to examine the ferroelectric characteristics of the materials, field dependence of polarization (P–E loops) was traced at room temperature using P–E loop tracer of M/S

Marine India Co Ltd of the electrically poled (medium silicon oil, dc field of 2.5 kV/mm) samples

3 Results and discussion

3.1 Crystal phase analysis

The X-ray diffraction (XRD) patterns of BGFBT, BFO and BT has been compared in the Fig. 1. From the XRD patterns, it is evident that the prominent peaks are found mostly equivalent with respect to its position and intensity like those of an ideal perovskite structure. Hence, it can be concluded that all the materials have been formed in a single-phase perovskite. BGFBT is a rhombohedral distorted cubic perovskite. Earlier report suggests that the association of *6p* and *6s* orbital of Bi^{3+} triggers a crucial ambience in inducing octahedral distortion [12]. In BGFBT the distortion established by the mutual rotation of an octahedral structure oriented in the (111) direction. The inclusion of Ba^{2+} at the *Bi*-site reduces the motion of *Bi* ion as well as hampers the structural distortion [18]. The XRD pattern of BGFBT shows the splitting of some higher angle reflection peaks which concludes the formation of rhombohedral phase. The larger atomic radii of Ba^{2+} (1.35 Å), as compared to that of Bi^{3+} (1.03 Å), might also be another responsible factor for peak shift as Fe^{3+} (0.64 Å) and Ti^{4+} (0.605 Å) have almost same ionic radii [19]. The prominent peaks of the patterns (matching with $BiFeO_3$ and/or $BaTiO_3$) were summarized with 2θ values of diffraction peaks using a standard computational package "POWD" and used to find out the phase of samples [20]. Based on the best agreement (using least square refinement sub-routine programme) between

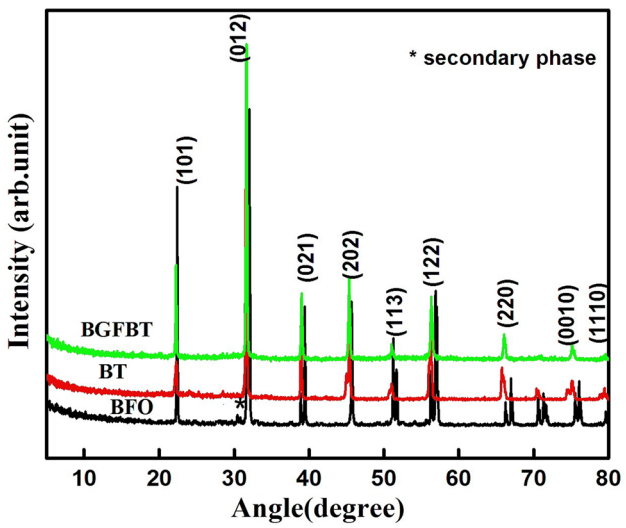

Fig. 1 Powder x-ray diffraction profile of BGFBT, BT and BFO at room temperature

observed (obs) and calculated (cal) value of the inter-planar spacing *d* (i.e., $\sum \Delta d = d_{obs} - d_{cal.} =$ minimum), structural phase was investigated. With refined lattice parameters, each peak of the pattern was finally indexed for all the samples. Using Scherer's formula the crystallite size (*P*) of the sample has been calculated; $P = (0.89\ \lambda)/\beta \cos\theta$, where ß refers to broadening (full width at half maxima = FWHM) of a reflection peak (*h k l*), wavelength (λ) = 1.5406 Å and θ is Bragg's angle. The average crystallite size is found to be 46 nm. With the mixed possession of *Gd, Bi* and *Ba* at the A-site and *Fe* and *Ti* at the B-site, the peak broadening could be decided. No secondary phase is observed in the BGBFT sample and hence suggesting the formation of single phase without $Bi_2Fe_4O_9$, $Bi_{24}Fe_2O_{39}$, or $Bi_{25}FeO_{40}$ [21] however some degree of secondary phase is observed in the BFO sample. Hence, it is concluded that the Gd substitution in the solid solutions plays an important role in modification and stabilization of structural parameter of the BGFBT electronic system [22].

3.2 Microstructure

Figure 2 represents the scanning electron micrographs (SEM) of BGFBT along with its energy dispersive x-ray analysis (EDAX) spectrum of the sintered pellet. From the micrographs, it is observed that well defined and uneven grain distribution revels on the surface. From the EDAX spectrum it is evident that all the assigned elements have been present without any loss. Similarly which can be confirmed from the elemental table (inset table in the EDAX picture) from its atomic as well as weight percentage study. The high temperature sintering may be one of the possible reasons for abnormal/secondary grain growth. Some times when we prepare pellet using powder this powder may not purely uniform fine powder. So, when by taking this powder if we prepare pellet for sintering it is very hard to get the uniform grain morphology. Hence due to different size of powder it is one reason of abnormal distribution of grain. Second thing some time foreign particle or unreacted reagent may creates different grain size. As we did not notice any foreign element from the XRD as well as EDAX spectrum this reason may be discarded. Third reason is the grain overlapping of one grain on another is the reason of different grain during high temperature sintering process.

The substitution of Gd^{3+} at the Bi^{3+}-sites not only segregate grains at grain boundaries, but also stop grain growth [23]. It is a genuine fact that even with a small level of defects (voids and oxygen vacancies) in microstructure significantly modifies the physical and electrical properties of the ceramic samples. A small level of oxygen vacancies (formed by the absence of Fe^{2+}), might decrease the leakage current density, having a positive effect on their electrical properties [24].

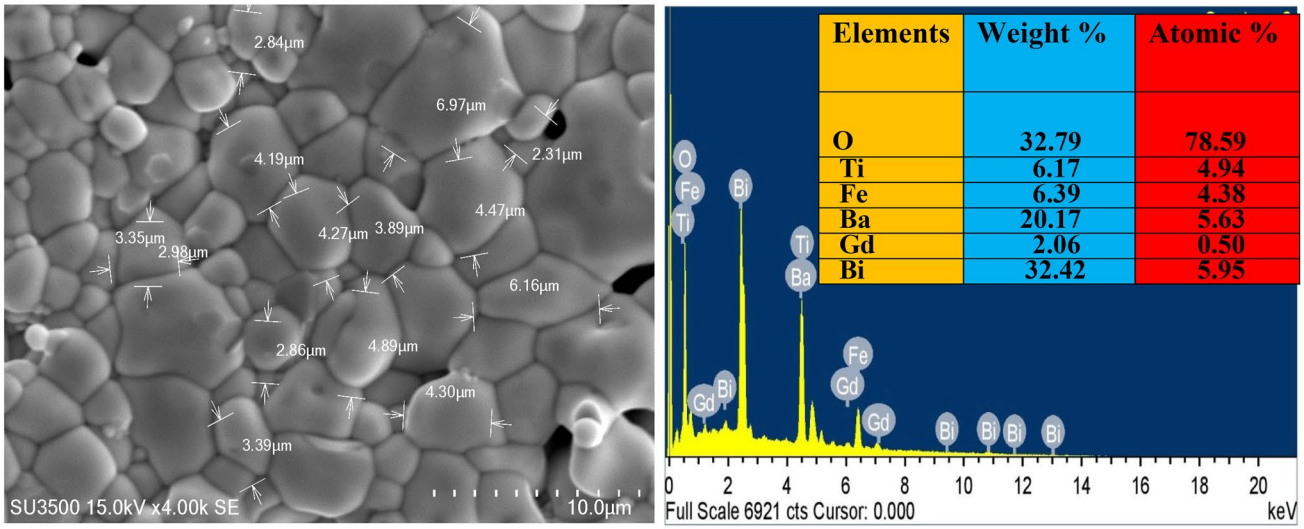

Fig. 2 Scanning electron microscope micrograph of BGFBT with its EDAX spectrum

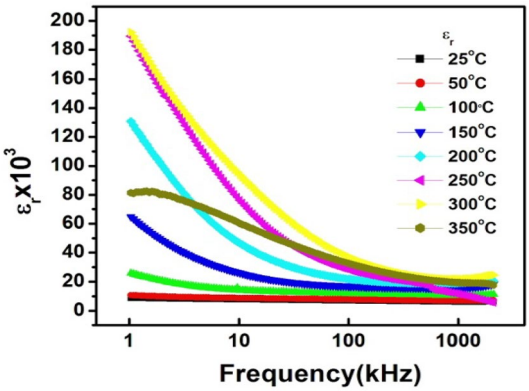

Fig. 3 Frequency dependency of relative permittivity of BGFBT

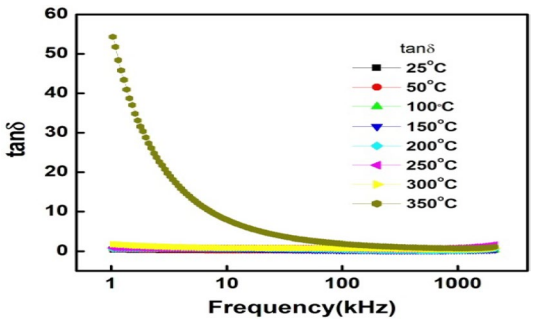

Fig. 4 Frequency dependency of tangent loss of BGFBT

3.3 Dielectric study

The frequency dependence of relative permittivity or dielectric constant (ε_r) and tangent loss (tan δ) of BGFBT, over a temperature spectrum ranging from room temperature to 350 °C has been presented in Figs. 3 and 4. As it is evident from the figure both dielectric parameters ε_r and tan δ decrease on increasing frequency which is a general feature of any dielectric material [25]. High-permittivity skew in the low frequency region on account of grain boundary impact whereas the high-frequency and low-permittivity locale manifests the indelible bulk impact. The relative permittivity response at low-frequency region of *Gd*-modified BGFBT concludes high esteems, as the temperature increases which can be explained on the basic mechanism of space charge polarization (supported by Maxwell–Wagner mechanism). As per that mechanism, the grain is seen to offer a similar low resistance and activation energy while the grain boundary has a generally low resistance and higher activation energy. Since, a conducting grain with an insulating grain boundary creates surface and internal barrier layer capacitor, it describes the high permittivity in the specimes [26, 27]. The origin of the polar region is caused by the structural distortion in the *Gd*-modified BGFBT solid solution. Because of the lattice matching of different sites of ions in the BGFBT solid solution, Gd^{3+} ions would enter in to the Bi-site of BFO. Which will lead to the formation of $(Gd^{3+}Bi^{3})O_{6}$ complexes at the Bi-site and breaks down the long-range interactions of polar BO_6 octahedral. The increase of Gd^{3+} substitution disrupts the ferroelectric long-range ordering, leading to an increase in compositional disorder, as a result, dielectric and ferroelectric characteristics of the samples change significantly. [28] The substitution of *Gd* and *Ba* at the *Bi*-site and *Ti* at the *Fe*-site of BFO, creates some oxygen vacancies and/or lattice distortion in the materials. Therefore, the formation of these defects during high temperature sintering ($2Fe_{Fe}+O_o \rightarrow 2Fe'_{Fe}+\ddot{V}_o+1/2O_2$) and

reduction of Fe^{3+} to Fe^{2+} may be one of the main reasons for high tangent loss in BFO [2]. The ionization of the oxygen vacancy designs to the mobile electrons in perovskite structure with *Ti*, which can be described as $V_o \leftrightarrow \ddot{V}_o + e'$ and $\dot{V}_o \leftrightarrow V_o'' + e'$. These electrons may be attached to Ti^{4+} in the form of $Ti^{4+} + e' \leftrightarrow Ti^{3+}$, and at that point, it is hard to clarify whether the weakly bonded electrons are situated close to V_o or *Ti* ions [29]. To control the volatile nature of Bi, *Gd* substitution is more effective as it suppresses the concentration of oxygen vacancies to modify the related dielectric parameters significantly. Due to high temperature sintering process and volatile nature of *Bi*, space charges and oxygen vacancies are created [30] as a result, the impact of ferroelectric domain wall pinning on the modification of physical properties of the materials may likely to be noticed. When Ba^{2+} is substituted at the Bi^{3+}-site then substitution of Ti^{4+} ion at Fe^{3+}-site is needed for charge balance, however oxygen vacancies is created owing to valence variation of *Fe* and *Ti* ions as Fe^{3+}–Fe^{2+} and Ti^{4+}–Ti^{3+} respectively [30].

The combined temperature-dependent relative permittivity (ε_r) and loss factor (tan δ) plots at suitable frequencies have been presented in Fig. 5. As evident from the figure that a typical frequency dispersion with a diffuse phase transition near the dielectric maximum temperature has been observed. This high flatter permittivity temperature response over a wide temperature range is surprisingly high as compared to previously reported data on Bi-based ceramics. The observed value remained higher than 10k of relative permittivity in the studied temperature range upto 400 °C, which is almost few order of magnitude larger than the well-known Bi- and $BaTiO_3$-based dielectric materials. The temperature stable dielectric permittivity along with low dielectric losses over wide temperature range(i.e., from room temperature to 300 °C some time it is referred as optimum working temperature of electronic devices) is mandatory for capacitor applications in worse atmospheric conditions and maintain a stable dielectric loss(i.e., less or equal to 1) over a wide range of temperature. However there is a significant increase in the value of dielectric loss at higher temperatures (> 300 °C) may be due to scattering of thermally activated charge carriers and presence of some unknown thermally activated defects (including oxygen vacancies) in the materials. At higher temperatures, the conductivity begins to dominate, which in turn, is responsible for rise in tangent loss [30].

3.4 Polarization hysteresis

$BiFeO_3$ is a displacive class ferroelectrics. In $BiFeO_3$, Bi^{3+} is a heavy ion and its *6s* orbital are more stable than *6p*. As a result, the large radial extension of the *6s* orbital lessens the overlapping of *6p* orbital of both + ve and −ve ions which implies the reduction of the bond strength. This splitting of energy *6s* and *6p* orbital causes hybridization and which ultimately leads to the polarization of the core *6s* electrons. The polarization of core electrons and reduction of structural distortion can be achieved by an addition of Ba^{2+} and Gd^{3+} (with its empty *p* orbital) at the Bi^{3+}-site. The reduced rhombohedra angle infers to decrease in lattice distortion [18]. Unlike $BiFeO_3$, the displacement of the transition metal ion takes place in $BaTiO_3$. As the dislodging of cations takes place in the (001) direction, it decreases the bond separation of Ti–O on one side, and expands on another side. Figure 6 compares the field dependence of polarization (P–E loop or hysteresis loop) of BFO, BT and BBGFBT at room temperature with working field of 150–200 kV/cm. As we know that the excellent insulation is mandate for absolute poling of the ceramics, as a result one may get more remnant polarization P_r. Similarly, it is a very hard task to create a dielectric breakdown under high field for the ceramics with excellent insulation [2]. Here, in BGFBT, the electrical insulation decreases with the creation of oxygen vacancies on the substitution of Ba^{2+}. This creation of oxygen vacancy will cause to oxygen octahedral distortion. On the other hand,

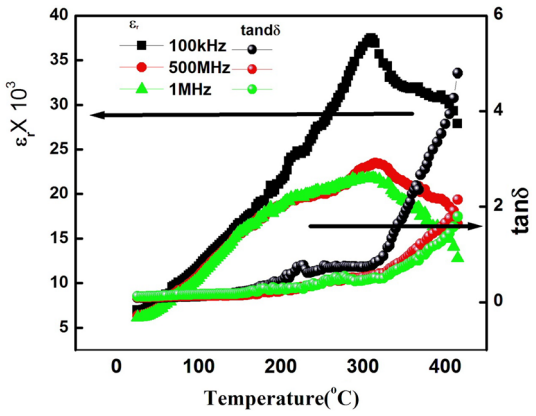

Fig. 5 Temperature dependency of dielectric parameters of BGFBT

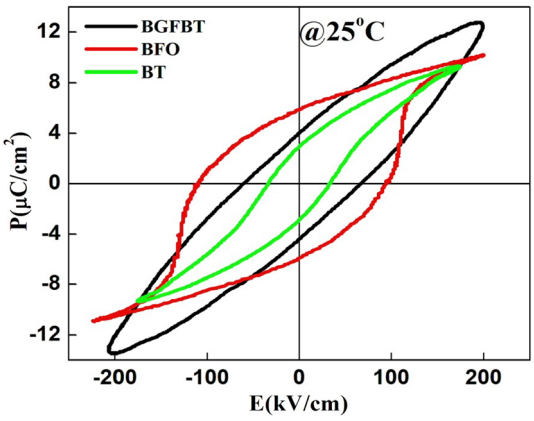

Fig. 6 Room temperature hysteresis of $BiFeO_3$, $BaTiO_3$ and BGFBT

the pinning effect on domains reversal is caused by oxygen vacancies, which indicates that the ferroelectricity of the ceramics is weaken after the inclusion of the excess di or tri valence ions. The value of the saturated polarization is found to be 10.269, 9.174 and 12.83 μC/cm^2 for BFO, BT and BGFBT respectively. Similarly the remnant polarization is found to be 5.97, 1.658 and 4.052 μC/cm^2 for BFO, BT and BGFBT respectively. It is an established fact that the ferroelectric polarization of bulk bismuth ferrite is along the diagonals of the perovskite unit cell (111), pseudo-cubic (001), and hexagonal [301]. The polarization vector is especially adjusted to major crystallographic directions [001] and [111] for tetragonal system (with space group P4mm) and rhombohedral (with space group R3m) symmetry separately. In a tetragonal ferroelectric phase, one-sixth of the domains are already arranged along the polar axis, another one-sixth is switched by 180° and remaining two-third is turned by 90° [31]. The coercive field is roughly 96.25, 35.289 and 68.119 kV/cm for BFO, BT and BGFBT system.

3.5 Electrical conductivity

Figure 7 presents the frequency dependence of ac conductivity of the materials at a various temperature band. $\sigma_{ac} = \omega\varepsilon\varepsilon_0 \tan\delta$ (where the parameters have their usual meanings) relation has been used to calculate the ac conductivity of the BGFBT, from the dielectric data. The activation energy E_a, derived from a thermally activated process has been estimated using the relation: $\sigma_{ac} = \sigma_0 \exp(-E_a/kT)$, where k = Boltzmann constant, and σ_0 = pre-exponential factor. Owing to different slant at different frequency region of the conductivity spectra we may conclude that the existence of multiple conduction processes with inconsistent activation energy [32]. Since, the conductivity is frequency dependent, it follows Jonscher's power law; $\sigma_{total} = \sigma_{dc} + A\omega^n$ [33] where σ_{dc} represents the very low (dc) frequency conductivity, A is temperature dependent constant and n is temperature dependent exponent within the range of $0 \le n \le 1$. The value of A indicates the quality of polarizability, whereas the value of n suggests the level of association of mobile ions with the lattices around them [34]. The value of n decreases with rise in temperature, whereas reverse trend is observed for pre-exponential factor A. The origin of the frequency-dependence of conductivity lies in the relaxation process and phenomena. When a mobile charge carrier hops from its original site to a new site, it remains in a state of displacement between two potential energy minima. In the meanwhile, the conductivity behaviour of the materials satisfy the universal power law; $\sigma(\omega) \alpha \omega^n$ with slope change dependent on n in the low-temperature region; $n < 1$ refers to the hopping process containing a translational motion with a sudden hopping of charge carriers, whereas $n > 1$ refers to the localized hopping without the species leaving the neighbourhood undisturbed [35–37]. The frequency at which change slope takes place, is known as hopping frequency of the polarons (ω_p), and also is temperature dependent. The high-frequency dispersion is ascribed to the *ac* conductivity whereas the frequency independent plateau region repents *dc* conductivity. Thus, studied materials satisfy universal power law. Figure 8 describes the temperature dependence of conductivity where with the help of thermal activation process the activation energy E_a, can be calculated using the relation: $\sigma_{ac} = \sigma_0 \exp(-Ea/kT)$, where k = Boltzmann constant and σ_0 = pre-exponential factor. In Fig. 8 for each frequency in the plot, there is the occurrence of different slopes in the different temperature bands suggests the presence of multiple conduction processes in BGFBT with different activation energy [6, 35].

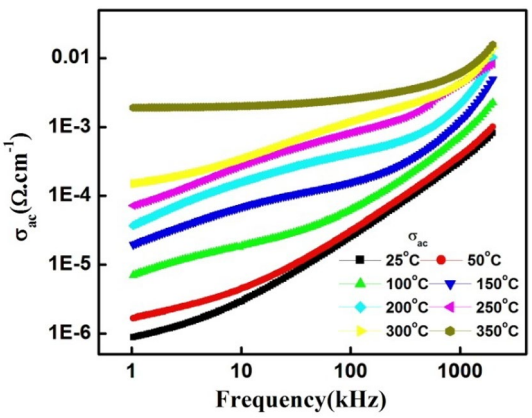

Fig. 7 Frequency dependent ac conductivity of BGFBT

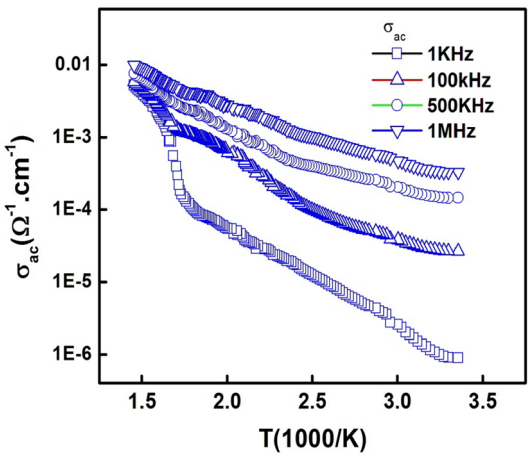

Fig. 8 Temperature dependent ac conductivity of BGFBT

3.6 Complex electrical modulus analysis

Figure 9a represents the frequency response of real part electrical modulus of BGFBT at few selected temperatures. From the figure it is obvious that the magnitude of M′ tends to zero, and coincide with each other in the low-frequency region in the temperature range beyond 150 °C, confirms the negligibly small contribution of electrode effect [35]. However there is small contribution of electrode effect up to temperature range 150 °C. The value of M′ increases with rise in frequency and reached a constant value at higher frequencies. The M′ variation with respect to frequency comprises features, such as (i) a very low value of M′ in the low-frequency region and (ii) a continuous dispersion with frequency having a tendency to saturate at a maximum asymptotic value in the high-frequency region for all temperatures. These observations can be related to a lack of restoring force governing the mobility of charge carriers under the action of an induced electric field at high temperatures. It may be due to difference in relaxation processes, which spreader over a wide range of frequencies. Figure 9b represents the frequency response of imaginary part electrical modulus of BGFBT at few selected temperatures. This showed that M''_{max} shifted towards higher frequencies side on increasing temperature suggesting a good correlation between motions of mobile ions. The M''_{max} shifted towards higher frequencies side. The peaks are broader and asymmetric on both sides of maxima. The asymmetric peak broadening indicates the spread of relaxation times with different time constant [6].

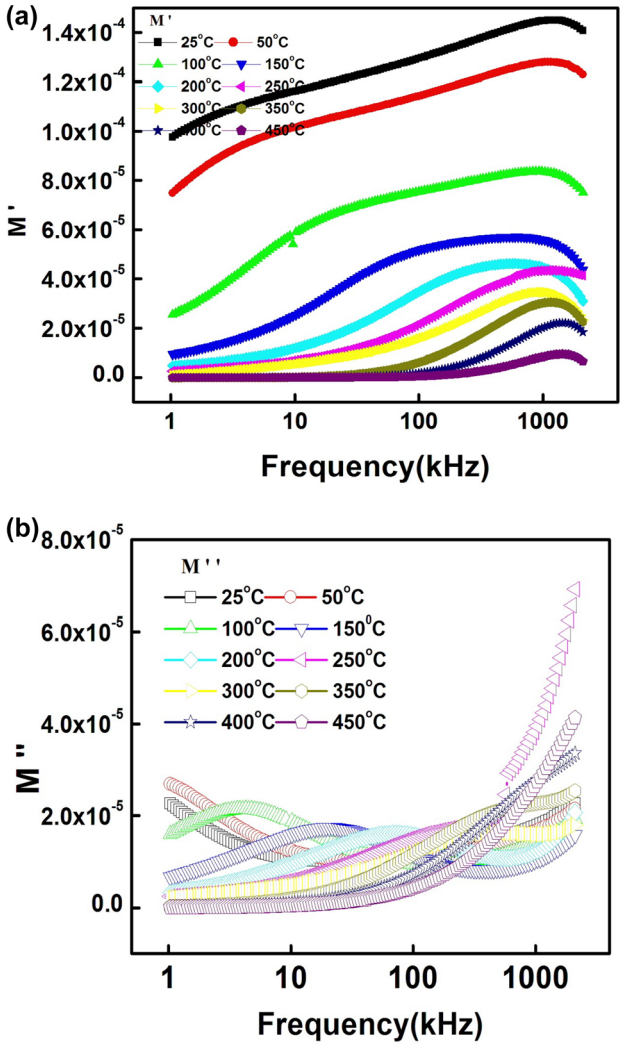

Fig. 9 **a** Frequency response of real part of electrical modulus of BGFBT. **b** Frequency response of imaginary part of electrical modulus of BGFBT

3.7 Complex electrical impedance analysis

Figure 10a, b depicts the frequency response of real and imaginary part of impedance respectively at different temperatures of BGFBT. It is found that Z′ has higher value at lower frequencies as compared to that of the

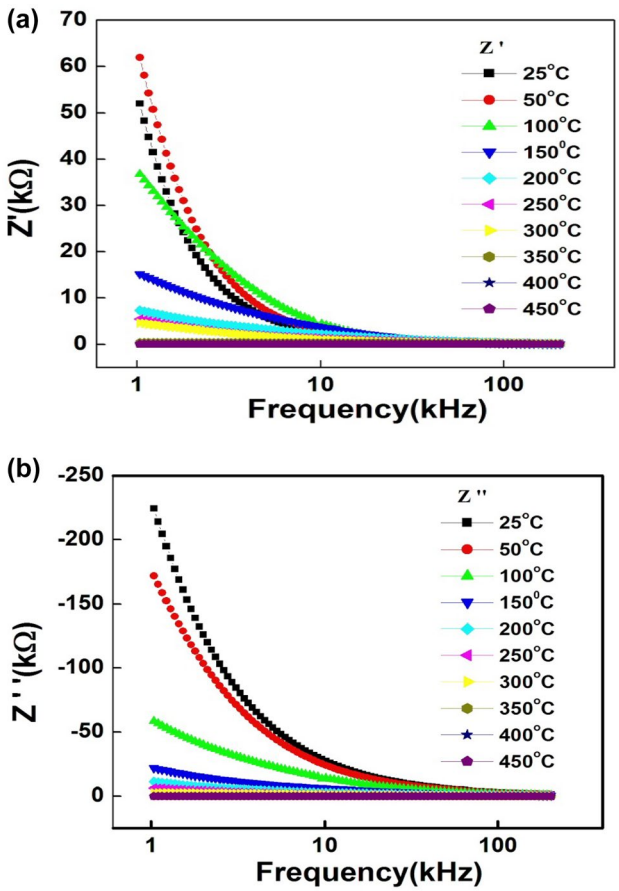

Fig. 10 **a** Variation of real part of impedance with frequency of BGFBT at different temperature. **b** Variation of imaginary part of impedance with frequency of BGFBT at various temperature

high-frequencies. It decreases slowly with increasing frequency, and then remains almost constant at higher frequencies and temperatures. As the value of Z′ of all the temperatures merges at high frequency, the release of space charge is expected. The Z″-frequency plots show characteristic peaks ($\omega_{max} = 2\pi f_{max}$) for the above solid solution which is not within the studied frequency range. The peak can also be related to the relaxation process, type, strength of the composites and experimental temperature. The asymmetric peaks occur due to the existence of multiple relaxation processes, and thus considered as a non-Debye type. Z″ peaks shift to the high-frequency side of increasing temperature. It is clear that space charge has less time to relax, and thus recombination takes place at a faster rate. At higher frequency, as the space charge polarization reduces at high frequency, all the curves merge [6, 35].

4 Conclusion

The BGFBT solid solution has been prepared via a conventional but standard economical synthesis technique with pure phase in the R3c crystallographic symmetry. No secondary phase is observed in the *Gd*- modified solid solution suggesting that pure phase can be obtained with the suitable modification by rare earth. The high value of dielectric permittivity suggests the material for possible application in capacitive energy storage devices. The extracted and composition dependent ferroelectric and electrical properties suggest the material to be a potential candidate for multifunctional devices. With incorporation of *Gd* in BFO–BT the structure becomes simpler and favourable properties can be extracted for the device parameter and its tuning.

Acknowledgements Author (CB) is gratefully acknowledged the grant received from SERB, DST, Govt. of India (PDF/2016/001078 dated 26th July.2016) to carry out the research work.

References

1. W. Eerensten, N.D. Mathur, J.F. Scoot, Nature **442**, 759 (2006)
2. Y. Guo, P. Xiao, R. Wen, Y. Wan, Q. Zheng, D. Shi, K. Ho Lam, M. Liu, D. Lin, J. Mater. Chem. C **3**, 5811 (2015)
3. C.S. Tu, R.R. Chien, T.-H. Wang, J. Anthoninappen, Y.-T. Peng, J. Appl. Phys. **113**, 17D908 (2013)
4. Y. Wei, X. Wang, J. Zhu, X. Wang, J. Jia, J. Am. Ceram. Soc. **96**, 3163 (2013)
5. S. Unruan, M. Unruan, T. Monnar, S. Priya, R. Yimnirun, J. Am. Ceram. Soc. **98**, 3291 (2015)
6. S. Pattanayak, R.N.P. Choudhary, S.R. Shannigrahi, P.R. Das, R. Padhee, J. Magn. Magn. Mater. **341**, 158 (2013)
7. X.M. Chen, J.L. Wang, G.L. Yuan, D. Wu, J.M. Liu, J. Yin, Z.G. Liu, J. Alloys Compd. **541**, 173 (2012)
8. W. Dong, Y.P. Guo, B. Guo, H.Y. Liu, H. Li, H.Z. Liu, Mater. Lett. **91**, 359 (2013)
9. X.J. Xi, S.Y. Wang, W.F. Liu, H.J. Wang, F. Guo, X. Wang, J. Gao, D.J. Li, J. Magn. Magn. Mater. **355**, 259 (2014)
10. H.L. Zhang, W. Jo, K. Wang, K.G. Webber, Ceram. Int. **40**, 4759 (2014)
11. T.H. Wang, C.S. Tu, Y. Ding, T.C. Lin, C.S. Ku, W.C. Yang, H.H. Yu, K.T. Wu, Y.D. Yao, H.Y. Lee, Curr. Appl. Phys. **11**, S240–S243 (2011)
12. R.A.M. Gotardo, D.S.F. Viana, M. Olzon-Dionysio, S.D. Souza, D. Garcia, J.A. Eiras, M.F.S. Alves, L.F. Cotica, I.A. Santos, A.A. Coelho, J. Appl. Phys. **112**, 104112 (2012)
13. J. Walker, H. Ursic, A. Bencan, B. Malic, H. Simons, I. Reaney, G. Viola, V. Nagarajanand, T. Rojac, J. Mater. Chem. C **4**, 7859 (2016)
14. C. Behera, R.N.P. Choudhary, P.R. Das, J. Mater. Sci.: Mater. Electron. **25**, 2086 (2014)
15. X. Lu, W. Bian, Y. Li, H. Zhu, Z. Fu, Q. Zhang, J. Am. Ceram. Soc. **101**, 1646–1654 (2018)
16. X. Lu, W. Bian, C. Min, Z. Fu, Q. Zhang, H. Zhu, Ceram. Int. **44**, 10028–10034 (2018)
17. P. Kumar, M. Kar, A.I.P. Conf. Proc. **1536**, 1041 (2013)
18. M.M. Kumar, A. Srinivas, S.V. Suryanarayana, J. Appl. Phys. **87**, 855 (2000)
19. T.H. Wang, C.S. Tu, H.Y. Chen, Y. Ding, T.C. Lin, Y.D. Yao, V.H. Schmidt, K.T. Wu, J. Appl. Phys. **109**, 044101 (2011)
20. E. Wu, *POWD* (School of Physical Sciences, Flinders University South Bedford Park, Bedford Park, 1989)
21. M.W. Lufaso, T.A. Vanderach, M. Pazos, I. Levin, R.S. Roth, J.C. Nio, V. Provenzano, P.K. Schenck, J. Solid State Chem. **179**, 3900 (2006)
22. J.R. Cheng, L.E. Cross, J. Appl. Phys. **94**, 5188 (2003)
23. L. Zivkovie, V. Paunovie, M. Milijkovie, M.M. Ristic, Mater. Sci. Forum **518**, 229 (2006)
24. T. Zheng, J. Wu, J. Mater. Chem. C **3**, 3684 (2015)
25. J.C. Anderson, *Dielectrics* (Chapman & Hall, London, 1964)
26. D.C. Sinclair, T.B. Adams, F.D. Morrison, A.R. West, Appl. Phys. Lett. **80**, 2153 (2002)
27. V.I. Gibalov, G.J. Pietsch, Plasma Sources Sci. Technol. **21**, 024010 (2012)
28. Z. Cen, C. Zhou, H. Yang, Q. Zhou, W. Li, C. Yan, L. Cao, J. Song, L. Peng, J. Am. Ceram. Soc. **96**, 2252 (2013)
29. A. Chen, Y. Zhi, L.E. Cross, Phys. Rev. B **62**, 228 (2000)
30. J.E. Garcia, V. Gomis, R. Perez, A. Albareda, J.A. Eiran, Appl. Phys. Lett. **91**, 0429021 (2007)
31. Z. Dai, Y. Akishige, J. Phys. D **43**, 445403 (2010)
32. L. Bellaiche, A. Garcı´a, D. Vanderbilt, Phys. Rev. B **64**, 060103 (2001)
33. K.S. Kumar, C. Venkateswar, D. Kannan, B. Tiwari, M.S.R. Rao, J. Phys. D **45**, 415302 (2012)
34. A.K. Jonscher, Nature **267**, 673 (1977)
35. S. Pattanayak, R.N.P. Choudhary, R. Piyush, Das, J. Mater. Sci.: Mater. Electron. **24**, 2767 (2013)
36. G. Catalan, J.F. Scottt, Adv. Mater. **21**, 2463 (2009)
37. S. Chandarak, M. Unruan, T. Sareein, A. Ngamjarurojana, S. Maensiri, P. Laoratanakul, S. Ananta, R. Yimnirun, J. Magn. **14**, 120 (2009)